

Geometry of a DNA Nanostructure Influences Its Endocytosis: Cellular Study on 2D, 3D, and *in Vivo* Systems

Anjali Rajwar, Shravani Reddy Shetty, Payal Vaswani, Vinod Morya, Amlan Barai, Shamik Sen, Mahendra Sonawane, and Dhiraj Bhatia*



Cite This: *ACS Nano* 2022, 16, 10496–10508



Read Online

ACCESS |



Metrics & More



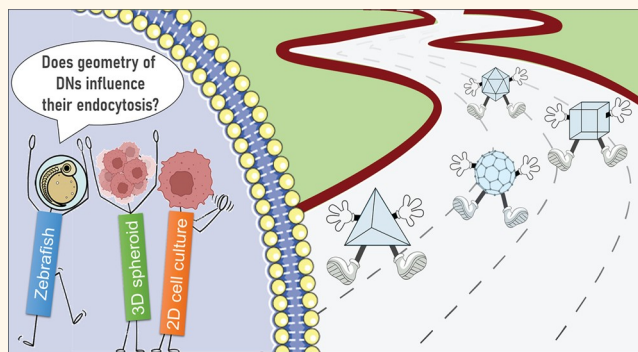
Article Recommendations



Supporting Information

ABSTRACT: Fabrication of nanoscale DNA devices to generate 3D nano-objects with precise control of shape, size, and presentation of ligands has shown tremendous potential for therapeutic applications. The interactions between the cell membrane and different topologies of 3D DNA nanostructures are crucial for designing efficient tools for interfacing DNA devices with biological systems. The practical applications of these DNA nanocages are still limited in cellular and biological systems owing to the limited understanding of their interaction with the cell membrane and endocytic pathway. The correlation between the geometry of DNA nanostructures and their internalization efficiency remains elusive. We investigated the influence of the shape and size of 3D DNA nanostructures on their cellular internalization efficiency. We found that one particular geometry, i.e., the tetrahedral shape, is more favored over other designed geometries for their cellular uptake in 2D and 3D cell models. This is also replicable for cellular processes like cell invasion assays in a 3D spheroid model, and passing the epithelial barriers in *in vivo* zebrafish model systems. Our work provides detailed information for the rational design of DNA nanodevices for their upcoming biological and biomedical applications.

KEYWORDS: DNA nanostructure, geometry, tetrahedron, 3D spheroid, *in vivo*, endocytosis



1. INTRODUCTION

DNA nanotechnology utilizes DNA as a structural material to construct DNA-based nanostructures with varying shapes and sizes by harnessing fundamental properties of DNA like orthogonality in base pairing and the ability to self-assemble into higher-order structures.^{1–3} Structural DNA nanotechnology has witnessed the groundbreaking developments in recent years in terms of realizing the nano-objects of practically any shape. Recent developments in software for structure prediction can guide the scientists not only to design different DNA-based objects, but also to determine the quantitative yields and in ways to minimize their off-target interactions.⁴ DNA nanostructures (DNs) have served as promising candidates for various biological and biomedical applications like drug delivery, biosensing, and other therapeutic applications owing to their inherent biocompatibility and low cytotoxicity.^{5–7} DNA nanotechnology utilizes small strands of DNA to create various 1D, 2D, and 3D nanodevices. DNAs are gaining increasing attention in scientific research due to the

ease of functionalization with moieties like peptides, small molecules, antibodies, aptamers, etc., and their ability to encapsulate various nanoscale cargo within their internal void.^{8–11} Despite such attractions, the actual applications of these devices have been limited in cellular and biological systems due to a lack of detailed investigations of such nanostructures within cellular and *in vivo* systems.

Cellular delivery of DNAs is crucial because once administered, these nanostructures must be internalized by cells in order to carry out their desired function. The study by Turberfield and colleagues demonstrated the internalization of DNA tetrahedra in live HEK cells guiding the potential for

Received: February 9, 2022

Accepted: June 10, 2022

Published: June 17, 2022



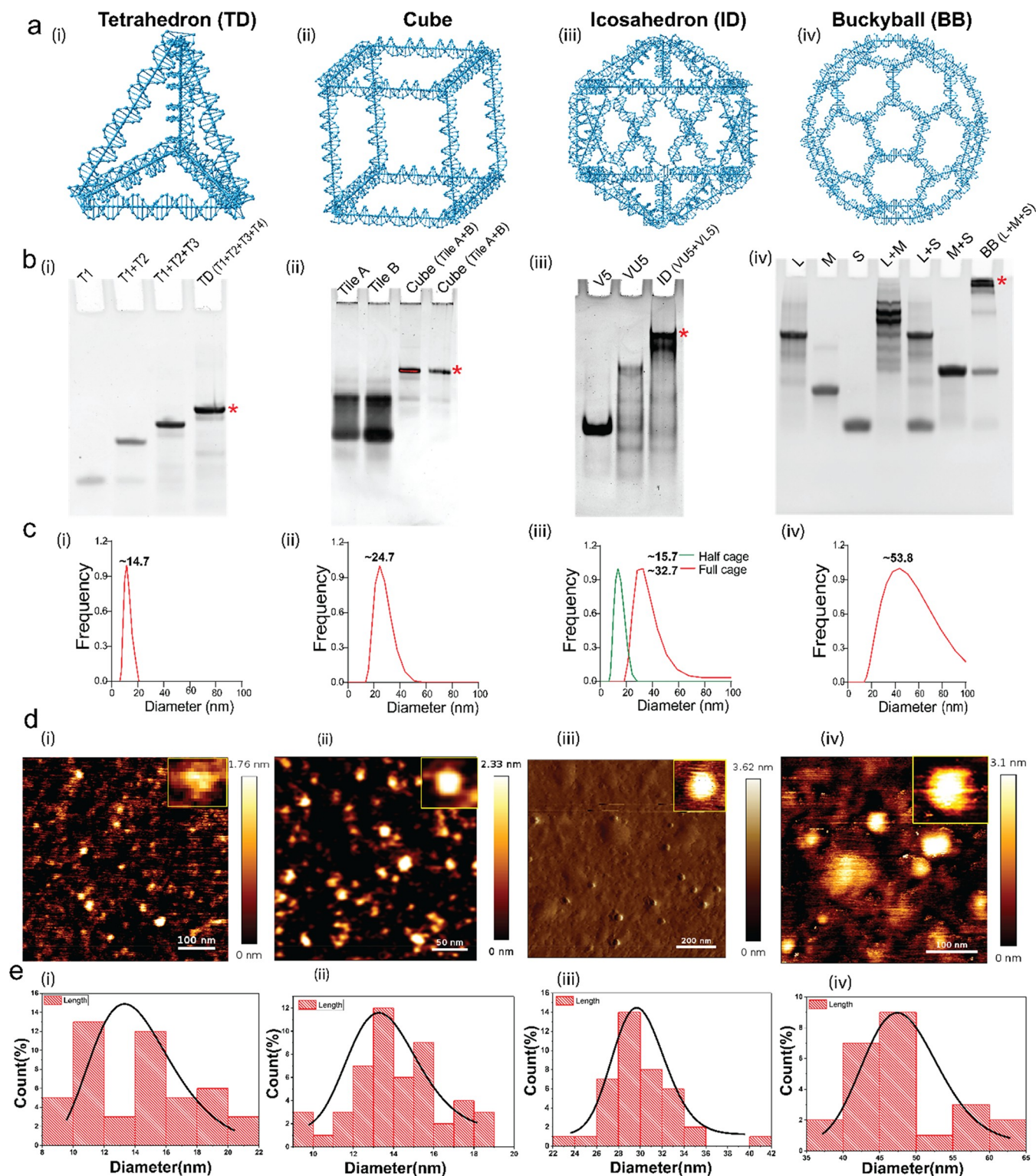


Figure 1. Design, preparation, and confirmation of DNAs. (a) Schematic illustration of DNA tetrahedron (TD), cube, icosahedron (ID), and buckyball (BB) drawn using the software Nanoengineer. (b) Gel-based characterization showing the retardation in the mobility upon formation of ordered 3D structures using 5% native-PAGE. (i) Formation of TD from four strands. (ii) Tile-based assembly of DNA Cube. (iii) Modular assembly of ID. (iv) Formation of BB from L, M, and S strands. (*) indicates complete structure. (c) DLS-based characterization showing the hydrodynamic diameter of structures formed shown in panel (b) indicating the correct sizes of the objects viz., TD \sim 14.7 nm, ID \sim 32.7, Cube \sim 24.4, and BB \sim 53.8 nm. (d) Representative AFM images of (i) TD, (ii) Cube, (iii) ID, and (iv) BB showing the topology of the objects formed in panel (e). Histogram represents the size distribution profile of DNA nanostructures measured from AFM. The average size of particles in TD is \sim 8–10 nm, Cube: 13–14 nm, ID: 28–30 nm, and BB: 45–50 nm.

utilizing DNAs for bioimaging and delivery of therapeutic agents into live cells.¹² The influence of geometry and size in the

internalization of DNA nanostructures has been partially explored.¹³ DNA origami nanostructures with various shapes

and sizes have been employed to deliver small molecules such as doxorubicin,^{14,15} different proteins such as nucleolin,¹⁶ antibody,^{17–19} and therapeutic nucleic acids such as siRNA,²⁰ CpG oligonucleotides²¹ into cells. Even modification of the backbone of DNA in nanostructures can favor accumulation at specific target tissue.²² However, significantly less research has been undertaken to reveal the influence of shape, size, and cell type in the cellular uptake process. The correlation between the topology and their internalization efficiency remains unexplored. In a study, Basting et al. have compared the internalization of different shapes of DNA origami structures with sizes ranging from 50 to 400 nm and found that more compact structures are preferentially internalized.²³ In a similar trend, most of the research carried out to investigate the design specific effect of DNAs has been limited to origami-based structures that have very high molecular weight compared to 3D DNA polyhedra.^{24,25}

We have studied herewith the interaction of 3D DNA nanocages of different geometries and sizes with the plasma membranes and their uptake pathways in cells. We have explored different geometries of DNA polyhedra such as DNA tetrahedron (TD), icosahedron (ID), cube, and buckyball (BB) and compared their cellular internalization. We have also studied the correlation between geometry and cell type specific internalization in multiple cell lines derived from various body tissues. To further understand the mechanism of cellular uptake of these DNAs, we have performed inhibitor studies to identify their endocytic route. Finally, we have demonstrated the internalization of DNAs using a 3D spheroid model and in the zebrafish embryos. We observe that of all the geometries explored, cell uptake was maximal in the case of TD. We further dissected the mechanism of endocytosis of DNA TD and found that uptake of it occurs majorly via clathrin-mediated endocytosis. Once getting uptaken into the cells, these cages trigger processes like cellular invasion in 3D spheroid models. A similar trend was observed in zebrafish embryos where DNA TD was efficiently getting internalized compared to other DNAs.

Here in this work we have demonstrated the geometry specific bias in the internalization of DNAs, their effect on cellular physiology like invasion in a 3D model and successful uptake in model animals. Our studies will establish key principles for future investigations involving DNA nanocages for biological applications specifically involving their surface topologies in the areas of bioimaging, drug delivery, immune activation, differentiations, etc.

2. RESULTS AND DISCUSSION

2.1. Design, Synthesis, Characterization, and Stability of DNAs. DNAs with different geometries were synthesized by utilizing the self-assembly property of the DNA molecule. Using previously published protocols, a panel of four structures comprising of different 3D polyhedral geometries like tetrahedron (TD),²⁶ icosahedron (ID),²⁷ cube,²⁸ and buckyball (BB)²⁹ were designed and constructed using a thermal annealing protocol in a reaction buffer containing 2 mM MgCl₂ in nuclease free water (Figure 1a). DNA TD was assembled using a single-step assembly approach from the equimolar ratio of four single-stranded oligonucleotides mixed in reaction buffer and annealed in the thermocycler. The reaction mixture was heated at 95 °C and then gradually cooled to 4 °C.³⁰ DNA ID utilized a modular assembly approach where different structures were synthesized sepa-

rately and assembled to form a complete structure.²⁷ Cube and BB were assembled using three-point star motif tiles as a building block.^{28,29} All the structures were labeled with cyanine-3 (Cy3) dye at their 5' end using one of the Cy3 modified ssDNA incorporated during the assembly process. DNAs were purified by gel electrophoresis and size-exclusion chromatography.

Electrophoretic mobility shift assay confirmed the formation of the structures with the desired stoichiometry of the component oligos due to its retarding movement in the gel (Figure 1b). AFM and DLS were explored to test if the bands with a lower mobility in gels correspond to the objects of desired size and dimensions. The hydrodynamic size and distribution of nanostructures were detected by dynamic light scattering (DLS). DLS studies showed the hydrodynamic diameter of TDs is 14.7 ± 3.8 nm, 32.7 ± 3.2 nm for IDs, 24.4 ± 2.4 nm for Cubes, and 53.8 ± 8.6 nm for BBs. These values fit perfectly well with the previously reported data of these structures^{26–29} (Figure 1c). The morphological characterization of the nanostructures was done using atomic force microscopy (AFM), which showed the characteristic shapes and sizes of the nanocages like TD, Cube, ID, and BB (Figure 1d).

The stability of DNAs is a very crucial parameter for utilizing these nanostructures in cellular and biological applications. DNA-based nanostructures are highly susceptible to nuclease degradation outside and inside the cells and can give deceptive fluorescence signals. To test the stability of DNAs to the cellular environment, we incubated all DNAs with 10% FBS, the component carrying nucleases. We found that all the DNAs were stable for up to 1 h (Figure S1 in the Supporting Information).

2.2. Concentration-Dependent Uptake of DNAs in Mammalian Cells. Cellular uptake of DNA constructs relies on transfection agents that help transport DNA across the negatively charged plasma membrane. However, DNA-based nanostructures are known to traverse the membrane of mammalian cells without any aid of transfection agents. In a previous study, Peng et al. have shown the interaction of three different shapes, i.e., tetrahedral, triangular prism, and cube, with the plasma membrane and observed that the corner angle of the nanostructure plays a critical role in their internalization.³¹ Intuitively, we have studied the cellular uptake of well-defined 3D DNAs (DNAs) with different topologies in the MDA-MB-231 breast cancer cell line. A concentration-dependent study (5 to 500 nM) was performed to identify the optimum concentration for further cellular studies. Cells were seeded 24 h before the experiment in DMEM media supplemented with 10% FBS. We studied the uptake of Cy3 labeled DNAs and Alexa488 labeled transferrin (Tf-A488) for 20 min at 37 °C. Tf-A488 is an endocytic marker of clathrin-mediated endocytosis that served as an internal control. The concentration of Tf-A488 used was 5 μg/mL and kept constant in all the experiments. The nontreated cells were considered as a negative control for validating the internalization efficiency of DNAs.

The internalization of nanostructure was characterized both qualitatively and quantitatively using laser scanning confocal microscopy. The internalization of DNAs was tracked using Cy3 conjugated DNA, which was incorporated during the assembly reaction. The concentration of Cy3-DNA was constant in TD and ID, whereas the number of copies of Cy3 DNA in cube and BB was more, which was normalized by dividing the total intensity by the number of fluorophores. The greater number

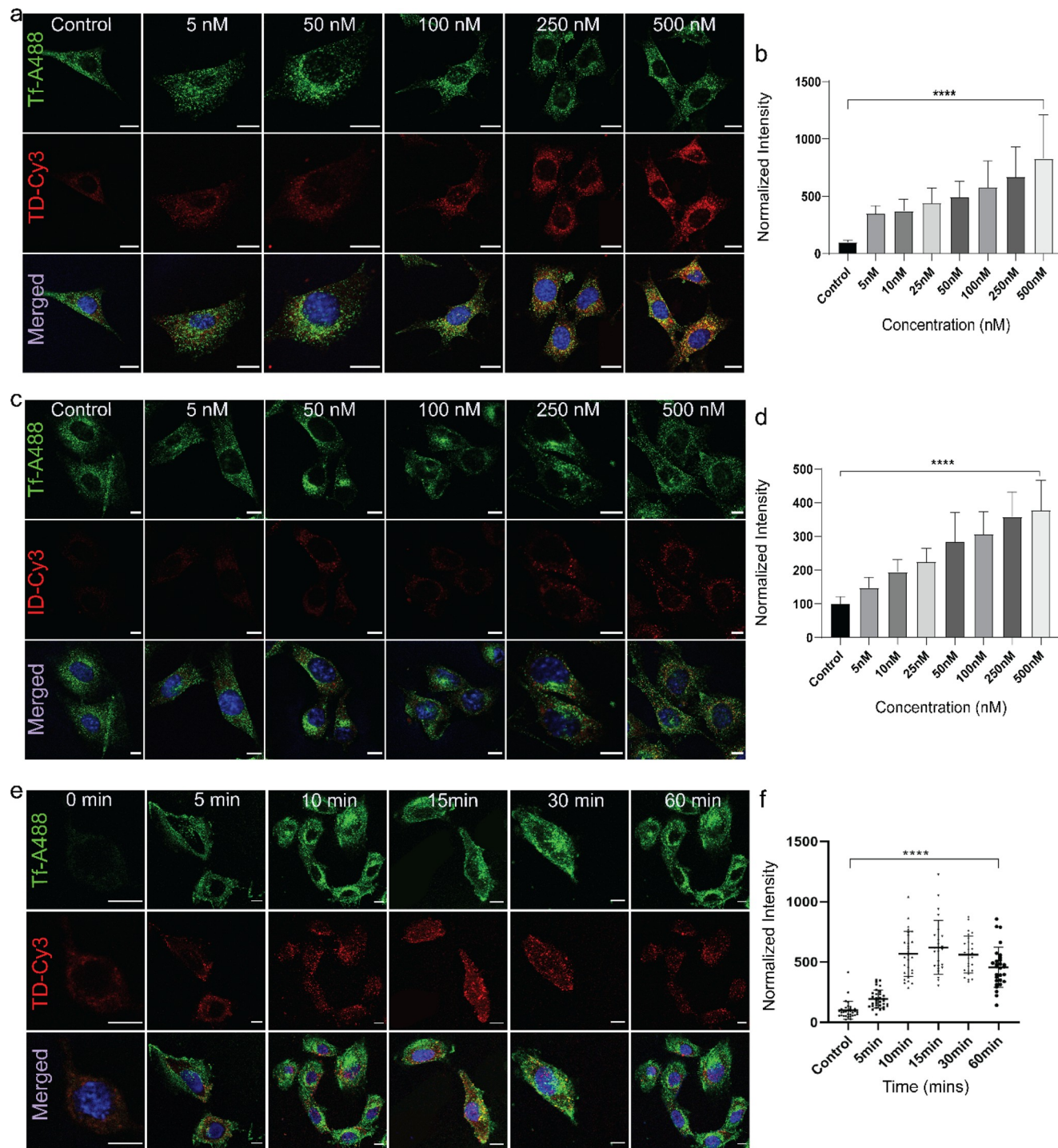


Figure 2. Cellular uptake of DNAs. (a,c) Confocal images of MDA-MB 231 cells treated with DNA TD-Cy3 and ID-Cy3 in different concentrations ranging from 5 to 500 nM. The green channel shows the uptake of TF-A488 (internal control), the red channel represents TD-Cy3 and ID-Cy3 uptake, and the bottom panel represents the merged images of all the channels with nuclei stained with Hoechst dye. Scale bar in panel (a): 15 μm . (b,d) Quantification of TD-Cy3 and ID-Cy3 uptake in MDA-MB231 cells from panels (a) and (c), respectively. (e) Time dependent study of DNA TD (150 nM) from 0 to 60 min. Green channel represents TF-A488. Red channel represents TD-Cy3 at different time points. (f) Quantification of TD-Cy3 uptake from cells in panel (e). The normalized intensity was calculated considering the average fluorescence intensity of the respective control as 100. Error bars in all quantifications indicate standard deviation. $n = 40$ cells per condition (ordinary one-way ANOVA, P value < 0.0001 ****) and ($N = 2$). Scale bar in panel (c) and (e): 10 μm .

of fluorophores in cube and BB are due to the inherent nature of these nanostructures. Their design comprises of repeating units, and each unit contains one fluorophore modified oligo, so the number of fluorophores are greater and required normalization. The nontreated cells showed negligible signals

in the red channel, validating that the fluorescence in the treated cells corresponds to the internalized DNAs. For TD, the signal can be detected at concentrations as low as 5 nM (Figure 2a,b), whereas for cube and BB the signal was visible only after 25 and 10 nM, respectively (Supporting Information,

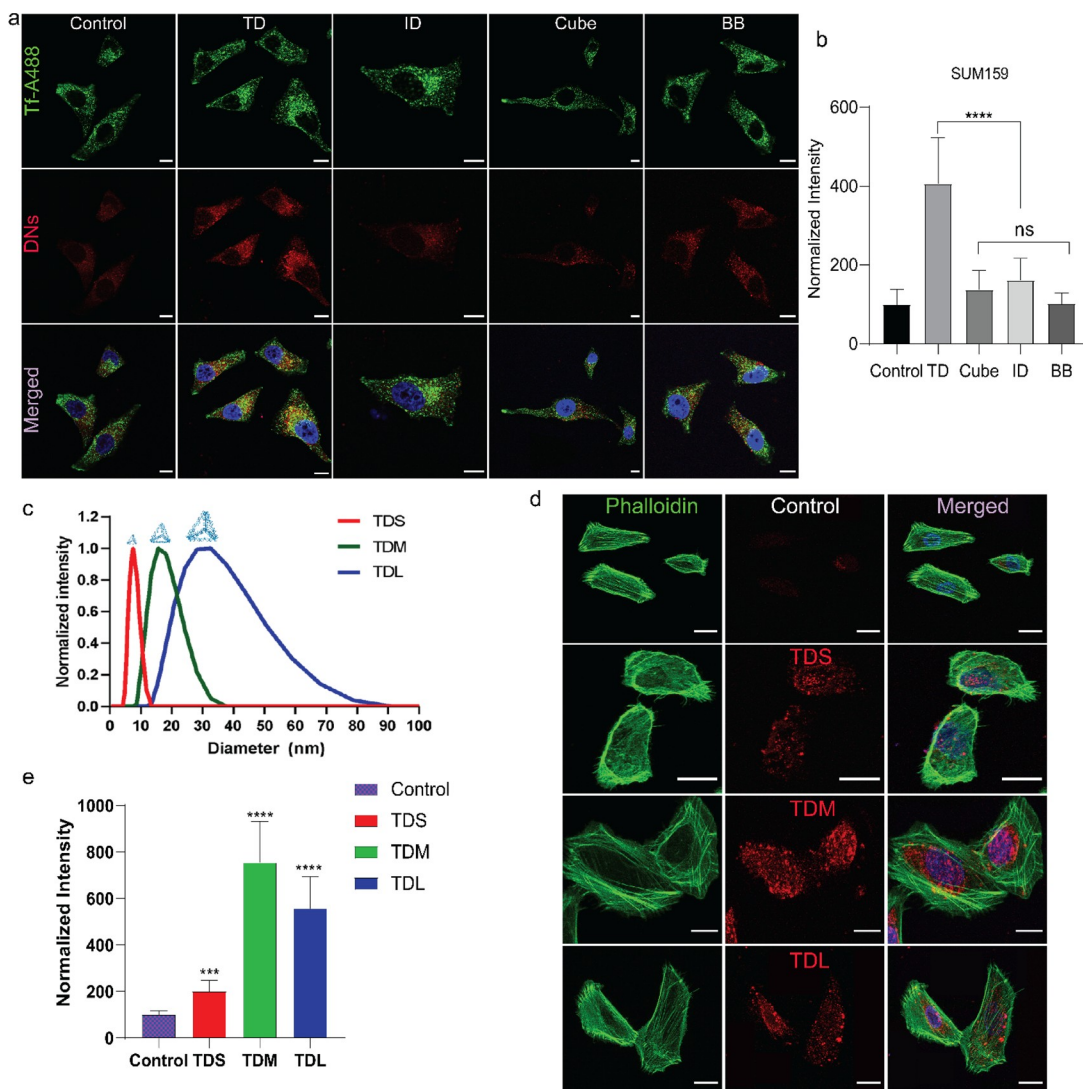


Figure 3. Effect of cell type and size in the uptake of DNAs. (a) Cellular uptake of TD, ID, Cube, BB in SUM 159 cells for 20 min at 37 °C. Confocal images of cells. The green channel represents the uptake of Tf-A488, the red channel represents Cy3 labeled nanostructure, and the bottom panel represents the merged image with nuclei stained with Hoechst. (b) Quantification of DNA nanostructure uptake in SUM159 cells from panel (a). Error bars in the quantification indicate standard deviation. The normalized intensity was calculated from 40 cells (ordinary one-way ANOVA, P value <0.0001 ****). (c) DLS based characterization of different sizes of DNA TD. The hydrodynamic diameter of small TD (TDS) ~ 11.7 nm, medium TD (TDM) ~ 14.3 nm, and large TD (TDL) ~ 32.7 nm. (d) Confocal images of SUM159 cells show DNA TD's size-dependent uptake at 150 nM concentration for 20 min at 37 °C. The green channel represents actin cytoskeleton stained with Phalloidin-A488, the red channel represents the different size of DNA TD, and the bottom panel represents the merged image with nuclei stained with Hoechst. (e) Quantification of the DNA TD internalization from cells in panel (d). TDM and TDL showed more internalization compared to TDS. Error bars indicate the mean of the two experiments with the associated s.d. (two-tailed unpaired t test; **** $p < 0.0001$, *** $p < 0.001$, *($N = 2$). Scale bar: 10 μ m.

Figure S2 and S3). However, ID's signal was significantly less than the other DNAs (Figure 2c,d). The signal of TD increases with the concentration, whereas for Cube and BB, the signal increases until 250 nM and then decreases, which may be due to either the aggregation of DNAs at higher concentrations or self-inhibition on the membrane due to crowding. The images were processed and quantified using ImageJ software. We further used 150 nM of DNA TD and conducted a time-dependent study (0, 5, 10, 15, 30, and 60 min) in parallel to study the cellular uptake over time. Initially, the intensity of TD from cells increased with time up to 15 min, after which it started to decrease, indicating the recycling of the internalized TD from the cells (Figure 2e,f). The intracellular fluorescence can be deceptive if proper controls are not considered. The use

of dye labeling to track DNA nanostructures has been shown to generate artifacts like free dye, or fluorophore modified oligo can also give false fluorescence signal.³² In order to nullify the fluorescence from any free fluorophore or ssDNA, we have compared the cellular intensity from fluorophore labeled ssDNA and free fluorophore as control. The signal from free dye and fluorophore labeled component strand was very negligible at the same concentration, demonstrating that the signal in the DN treated sample is due to the intact structure and not because of free dye or component strands. The results are included in the Supporting Information as S12 and S13.

2.3. Cellular Uptake of DNAs Is Size and Cell Type Dependent. How different DNAs bearing different topologies interact with complex cellular environments of different cell

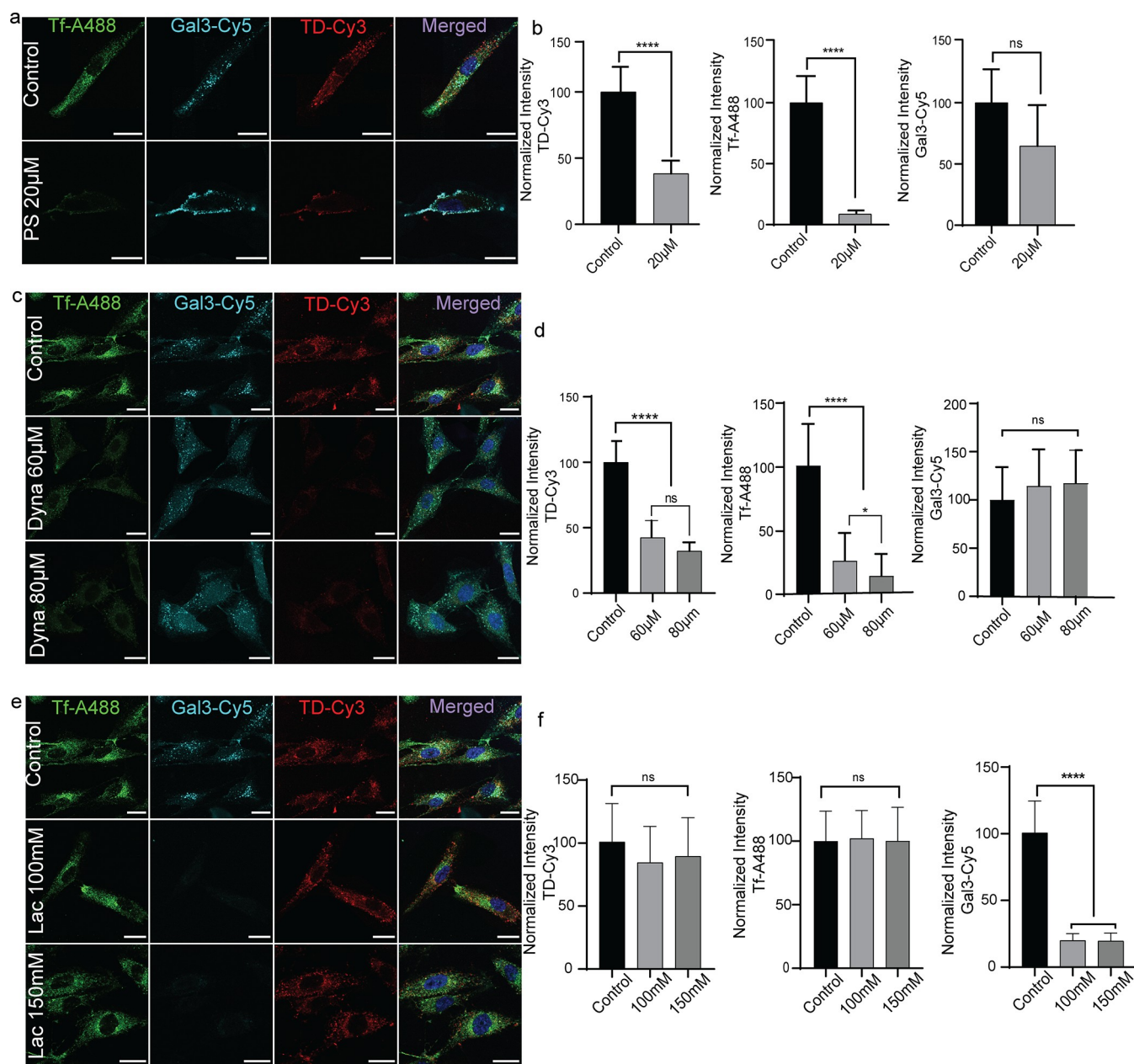
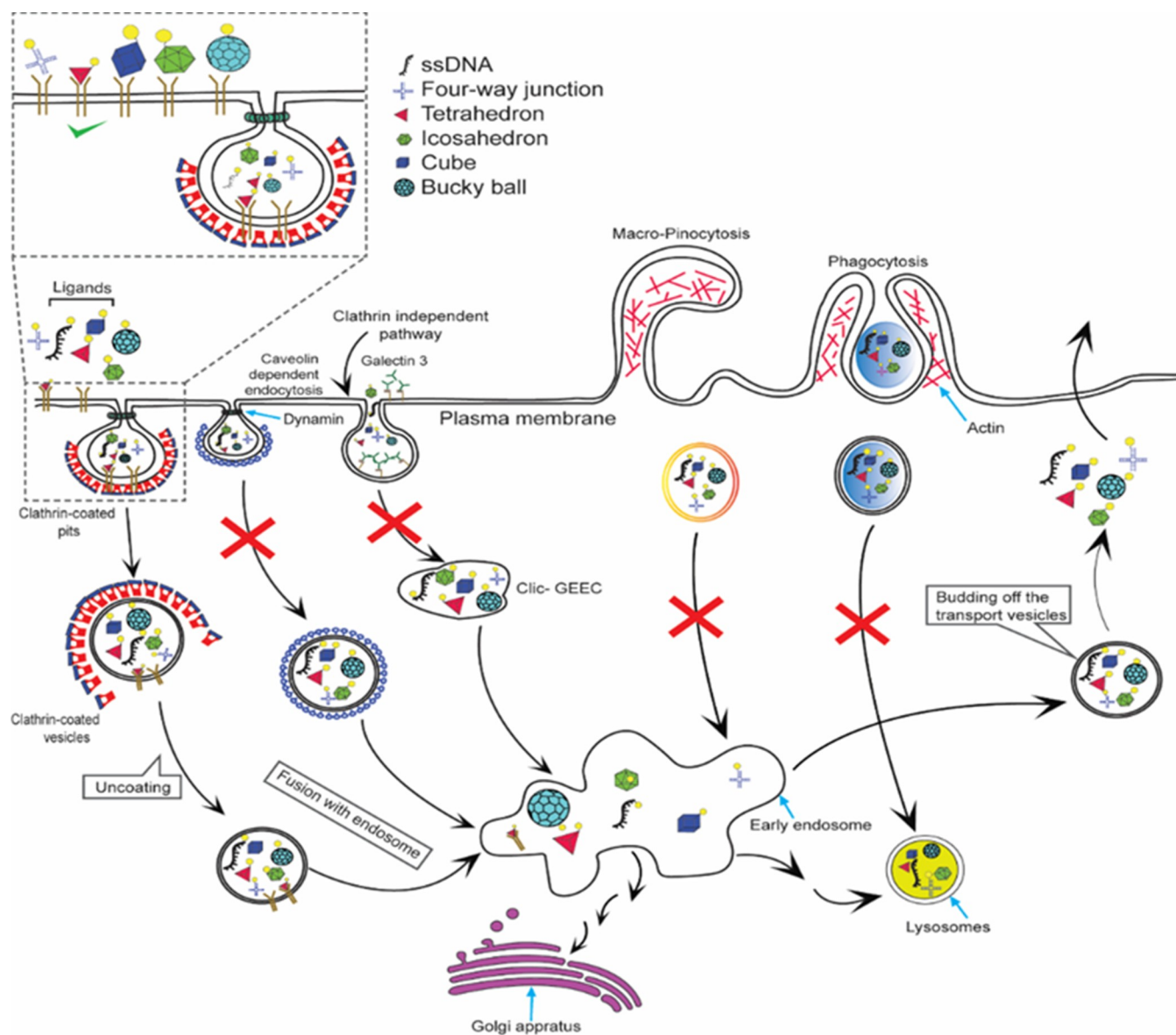


Figure 4. DNA TDs get endocytosed by clathrin mediated endocytosis in mammalian cells. (a) Confocal images of Rpe1 cells showing the uptake of Tf-A488 in the green channel, Galectin3-Cy5 in the cyan channel, and TD-Cy3 in the red channel for 20 min at 37 °C in the presence or absence of 20 μ M Pitstop-2. (b) Quantification of inhibition of CME pathway by Pitstop-2 for Tf-A488, TD-Cy3, and Gal3-Cy5 from cells in panel (a). Significant inhibition of TD and Tf but not significant inhibition of Gal3. (c) Blocking the dynamin-dependent pathway by inhibiting the dynamin via Dynasore inhibitor at 60 μ M and 80 μ M concentrations. The cellular uptake of TF-A488, Gal3-Cy5, and TD-Cy3 was monitored with and without the treatment of Dynasore for 20 min at 37 °C. (d) Quantification of inhibition by measuring the fluorescence intensity of TF-A488, TD-Cy3, and Gal3-Cy5 with and without treatment for Dynasore from cells in panel (c). The uptake of TD and Tf were significantly inhibited at both of the concentrations, whereas the uptake of Gal-3 was not very significantly affected. (e) Uptake of Tf-A488, Gal3-Cy5, and TD-Cy3 with inhibition of CIE pathway by Lactose. (f) Quantification of inhibition of CIE pathway for Tf-A488, Gal3-Cy5, and TD-Cy3. Significant inhibition of Gal3-Cy5, but no significant inhibition of TD-Cy3 and Tf-A488. For all quantifications, error bars indicate the mean with associated s.d. (two-tailed unpaired *t* test; **** $p < 0.0001$, * $p < 0.05$, ns: nonsignificant) and (*N*) = 2. Scale bar: 10 μ m.

types can be utilized to provide a unified piece of information about the cell-specific preference of DNs. The type of cell line also plays a vital role in the internalization of DNA nanostructures. Smolková et al. have demonstrated the effect of cell size in the internalization of DNA nanostructures where they found linear correlation between cell area and uptake.³³ We studied the uptake of DNs in a panel of cell lines

originating from different sources and body tissues including SH-SY5Y, HeLa, SUM159, KB3, and RPe1. We found 150 nM is the optimum concentration to study the cellular uptake from the previous experiment and was used for further experiments, as at lower concentration some DNs were not showing significant fluorescence signal. DNs of different geometries were uptaken with varying efficiencies in SUM159 cells (Figure

Scheme 1. Internalization Pathway Potentially Followed by Tetrahedral DNA in Cells^{4f}

^{4f}Multiple pathways coexist at the plasma membrane for internalization of various cargos including nutrients, growth factors, toxins, and even fluid. We successfully marked two different endocytic pathways viz clathrin dependent and independent pathways and we found that DNA nanocages of different geometries mostly adopt the clathrin mediated endocytosis. Further, the uptake of these nanocages is strongly correlated with the object's geometry, and we found that only tetrahedral geometry is more preferred for uptake in cells and in vivo.

3a,b) and other cell lines as well (Supporting Information, Figure S4, S5, S6, and S7). We found that DNA TD's uptake was higher than other DNAs in all the cell lines. We further compared the internalization of TD in different cell lines to investigate if there is any tissue specific preference in the internalization of DNA TD. We found that the internalization of TD was more in the cancerous cell lines compared to the noncancerous cell lines. Among the cancerous cell lines the internalization was maximum in breast (SUM159), kidney (HEK293T), and liver (WRL) cell lines (Figure S8).

Since DNA TDs were getting internalized in all the cell types with maximum efficiency, we further investigated if the size of TD has any role to play in the internalization of DNA TDs. TDs of three different sizes were synthesized using thermal annealing protocol as described previously. The hydrodynamic size of TD was analyzed by dynamic light scattering and found

to be 11.7 nm for small TDs (referred to as TDS), 14.3 nm for medium TDs (referred to as TDM), and 32.7 nm for large TDs (referred to as TDL) (Figure 3c). We also did the gel and AFM based characterization to confirm the sizes of DNA TD of different sizes (Figure S16). We did the cellular uptake studies in the SUM159 cell line at a 150 nM concentration of TD. We hypothesized that TDS will be internalized more owing to its smaller size, but in contrast, we found that TDM followed by TDL has shown maximum internalization (Figure 3d,e). This explains that the size of the ligand indeed has a vital role to play in the internalization of DNAs.

2.4. DNA TDs Get Endocytosed by Clathrin Mediated Endocytosis. Efficient cellular uptake of the cargo is the primary requirement for delivering molecules of interest. Previous studies have demonstrated that different DNA nanodevices like i-switch^{34,35} and DNA icosahedron³⁶ get

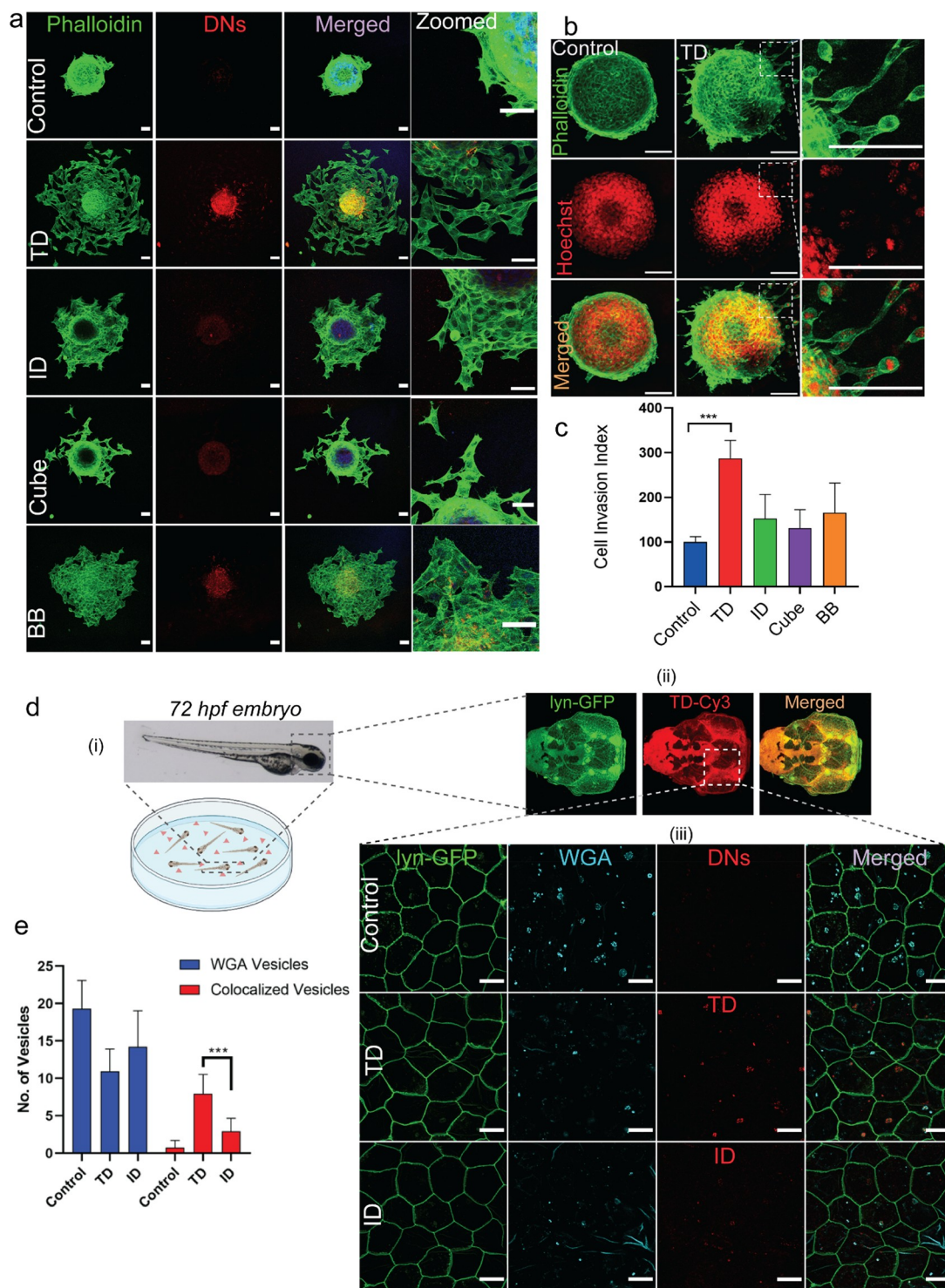


Figure 5. DNA TDs stimulate 3D cell invasion in the spheroid model and in vivo uptake in the zebrafish model system. (a) Confocal images of DN uptake by MDA-MB231 spheroids after 24 h of incubation at 37 °C. DNs have shown invasion in 3D spheroids as cells showed migration from the spheroid core. The green color represents phalloidin staining of actin filaments, red color represents Cy3 labeled DNs. Scale bar: 50 μ m. (b) Magnified images of 3D spheroids. Nontreated spheroids were considered as control. TD has shown maximum invasion followed by BB. Scale bar: 50 μ m. (c) Quantification of cellular invasion from spheroids shown in panel (a). Cell invasion index was calculated by measuring the migration distance by cells from the spheroid core. For each nanostructure, a minimum of 8 spheroids were quantified and (N) = 3. Error bars indicate standard deviation (ordinary one-way ANOVA, *** p -value < 0.001). (d) In vivo uptake of DNs in the zebrafish embryo. (i) Schematic of experimental design. 72 hpf zebrafish embryos were soaked in media containing 300 nM of DN and incubated for 4 h. (ii) Confocal images of the dissected head of 72 hpf embryo showing the internalization of TD shown in red color. Green color represents membrane-tethered lynEGFP. (iii) Confocal images of the peridermal cells of zebrafish embryo showing the internalization of DNs. Scale bar: 15 μ m. (e) Quantification of DNs internalized into the peridermal cells, calculated by counting the number of DN vesicles colocalized with WGA vesicles, which is known to mark endocytosis in general. Error bars indicate the mean with associated s.d. (two-tailed unpaired t test; *** p < 0.001). For each condition, n = 6–8 embryos were quantified and (N) = 2.

internalized via scavenger receptors in cells and coelomocytes of nematode *C. elegans*. We optimized the uptake of different DNs and concluded that of the tested geometries, TDs are most efficiently internalized in all the cell types. We further wanted to delineate the cellular pathways involved in the internalization of DNA TDs. The uptake of small ligands into cells takes place mainly via active processes like endocytosis via interactions with specific receptors. There are two major pathways for endocytosis broadly classified into clathrin-mediated endocytosis (CME) and clathrin-independent endocytosis (CIE) involving the clathrin machinery. Alternatively, less efficient modes such as phagocytosis are involved in the uptake of large sized structures like bacteria. However, these are not very efficient and are very slow in action.

Since DNA TDs are ligands of size 15 nm, we ruled out the phagocytosis and used inhibitors to block the CME and CIE pathways. Pitstop-2 is a well-studied inhibitor of the CME pathway, which interferes with the terminal domain of clathrin involved in coated pit dynamics, thereby inhibiting clathrin pit scission from the membrane and blocking vesicle transport to the endosome.³⁷ Lactose has been shown to compete with lectins like galectin-3, which binds the glycosylated receptors thereby blocking the formation and uptake of clathrin independent carriers.³⁸

Cells were pretreated with two different concentrations of Pitstop-2 (20 μM and 40 μM) to block the CME process for 15 min at 37 $^{\circ}\text{C}$ specifically. Control cells and treated cells were probed to check the uptake of TD-Cy3, Tf-A488, and Gal3-Cy5 after 20 min of incubation at 37 $^{\circ}\text{C}$. For pitstop-2 treatment, two different concentrations were tested, and the pathway got inhibited at 20 μM ; however, the cells got stressed at 40 μM . Transferrin is a well-established marker for the CME pathway and thereby was used as a positive control. Galectin-3, known to enter the cells via the CIE pathway, was used as a negative control for Pitstop-2. The CME pathway got inhibited upon treatment with 20 μM of Pitstop-2, as confirmed by the quantitative reduction in the signal of Tf-A488, whereas the uptake of Gal3-Cy5 was not significantly affected. The signal from TD was significantly reduced, suggesting the internalization of TD by the CME pathway (Figure 4a,b).

We used another inhibitor, "Dyasore", to block the CME pathway to further confirm the above results. Dyasore inhibits dynamin that acts as a molecular scissor and regulates the dynamics of clathrin-coated vesicles.³⁹ Dyasore inhibits the GTPase activity of dynamin, which is involved in the pinching of the vesicles. The CME pathway was blocked by pretreating the cells with 60 and 80 μM concentrations of Dyasore for 30 min. Again, TD uptake was significantly affected along with Tf-A488, suggesting CM-dependent endocytosis of TDs (Figure 4c,d). However, the internalization of Gal-3 was not severely affected. In contrast, the uptake of TDs remains unaffected mainly in cells pretreated with lactose, a known competitive inhibitor of galectins that blocks the CIE pathway⁴⁰ (Figure 4e,f). Taken together, these findings support a CME-dependent mechanism of TD internalization. We additionally checked the internalization route of TD in MDA-MB231 cell lines and observed the similar trend results; i.e., upon treatment with pitstop-2 and Dyasore, the internalization of TD was significantly reduced. In contrast, upon lactose treatment the internalization of TD was unaffected, inferring the internalization of TD via CME process (Figure S9, S10). Previous reports suggested the internalization of many DNs via the caveolin pathway. We employed methyl beta-cyclodextrin

(m β CD) inhibitor to selectively block the caveolin pathway.⁴¹ We found that the internalization of TDs was not significantly disturbed upon treatment with m β CD, whereas the uptake of CtxB, a potential cargo for caveolin pathway, was selectively inhibited⁴² (Supporting Information, Figure S11). However, caveolin mediated uptake is present mainly in muscle cells, and its expression is minimum in other body cells, whereas clathrin mediated and independent pathways are ubiquitous in all body cell types. Taken together, these findings suggest that TD follows the Clathrin pathway to enter the cells as shown in Scheme 1.

2.5. DNA TDs Stimulate 3D Cell Invasion in Spheroid Model and in Vivo Uptake in Zebrafish Model System.

3D cell culture mimics cells' physiological environment and thus provides an improved platform to study cellular spreading, migration, and invasion, as well as differentiation. In 3D cell culture, cells clump together to form stable cell-to-cell contacts, thereby maximizing the communication and signaling between the cells. MDA-MB-231, extremely aggressive triple-negative human breast cancer cells, were used to prepare 3D spheroids using the hanging drop method. It is a non-scaffold-based method in which cell suspensions are placed dropwise on the lid of the Petri dish.⁴³ The cells aggregate due to gravity and form a compact spheroid at the base of the drop after 36 h of culture at 37 $^{\circ}\text{C}$. These spheroids can then be transferred to the collagen matrix to invade the 3D system. This invasion potential of the cells can be either stimulated or inhibited by using specific activators or inhibitors. We wanted to check if DNs had any effect on the invasion potential of these spheroids. Spheroid invasion assay provides an attractive platform to study the invasion potential of 3D DNA-based nanodevices. Cell invasion potential can be quantified by measuring the dispersion of cells in different directions or by calculating the migration distance covered by cells from the intact spheroid core. Following the characterization of uptake of different DNs in the 2D cell culture system, we then investigated the uptake of DNs in the 3D spheroid models. To evaluate the invasion potential of DNs with different topologies, we incubated the spheroids with DNs for 24 h at 37 $^{\circ}\text{C}$. Untreated spheroids were considered as controls that showed minimal invasion potential, as the migration distance was negligible, and hardly any cells invaded out from the spheroid core into the collagen matrix (Figure 5a). The zoom-in image of the section of spheroids also demonstrated successful endocytosis of the DNA TDs into migrating cells, thereby stimulating their invasion (Figure 5b). Spheroids treated with DNs showed visible cell invasion in the matrix, the migration distance was greater, and many cells migrated in different directions away from the spheroid core. This could be due to the modulation in the signaling pathway such as Wnt-beta catenin, RhoA/ROCK2, etc., by DNs, which regulates the expression of genes involved in migration and cell proliferation.^{44–46} Cell migration is a key process in invasion that drives the movement of the cells from the spheroid core. The treatment with DNA tetrahedron is known to promote cell migration in stem cells by activating the RhoA/ROCK pathway and regulating the expression of certain noncoding RNAs and mRNAs involved in migration.⁴⁴ Among all, TD showed the maximum invasion, followed by BB, ID, and Cube (Figure 5c). The reason tetrahedral DNA showed maximum invasion can be owed to its preferential internalization compared to other cages. The greater the internalization, the greater are the chances of activation of downstream signaling

events involved in cell migration, thereby greater are the number of cells coming out from spheroid core upon treatment with DNA TD.

We further asked if the geometry of DNs has a similar impact on their uptake in the *in vivo* systems as was observed in cells. We tested this by performing an *in vivo* uptake assay of TD and ID in zebrafish embryos, as these DNs showed the maximum invasion potential in the previous experiment. The *in vivo* uptake of DNs was performed in zebrafish embryos obtained from a transgenic line *Tg(cldb::lyn-EGFP)* in which the expression of lynEGFP is driven by *claudin* promoter marking the membrane of peridermal cells. To check the entry of nanocages, 72 hpf (hours post fertilization) embryos were soaked in a solution containing 300 nM of DNs for 4 h (Figure Sd(i)), after which the embryos were washed, fixed, and imaged using confocal microscopy. Wheat germ agglutinin (WGA) was used as an internal control to show the potential of these DNs to overcome the mucus barrier and their successful uptake into the zebrafish peridermal cells. We observed that the internalization of TD was more compared to the ID and control (Figure Sd(iii)). Further quantification of the number of vesicles labeled by control, TD, and ID and colocalized with the WGA vesicles confirmed this trend (Figure Se).

3. CONCLUSIONS

DNs with different topologies, i.e., TD, ID, Cube, and BB, were synthesized and characterized using different biophysical techniques. We studied how these different DNs play crucial roles in interactions with membranes leading to their very specific uptake into mammalian cells. In this study we observed that DNs follow a Clathrin-mediated pathway to enter the cells. The Clathrin pathway is known to trigger the signaling cascade of MAPK, SRCK, which is known to regulate proliferation and migration in 2D and 3D.^{47,48} It is this active endocytosis of DNs into the cells that triggers 3D invasion of cells from spheroids into the collagen matrix. Not only do these nanoparticles show geometry bias in 3D cellular invasion, but also they possess the capacity to enter epithelial cells in *in vivo* systems like zebrafish embryos. Taken together, our results have established the strict influence of DN geometries on their interactions with biological systems. These results will play crucial roles in the future development of DNA based smart nanoparticles with specific and targeted capacities to probe and program biological systems for multiple applications like bioimaging, targeted delivery, activation of immune cells, or as scaffolds for tissue engineering, and many more.

4. MATERIALS AND METHODS

4.1. Materials. Dulbecco's Modified Eagle Medium (DMEM) was purchased from Lonza. DMEM-F12, HAMS-F12, Fetal bovine serum (FBS), PenStrep, Trypsin-EDTA (0.25%), and collagen were purchased from Gibco, and phosphate buffer saline (PBS) was purchased from HyClone. The sequences used for DNA nanostructure synthesis (Tables S1–S4 in the Supporting Information), 6× loading dye, 50 bp DNA ladder, mowiol, transferrin-A488, Cy5, Hoechst, Pitstop-2, Dynasore, methyl- β -cyclodextrin and Lactose were ordered from Sigma-Aldrich. Nuclease free water, ammonium persulfate, ethidium bromide, TEMED, triton-X, paraformaldehyde, and adherent cell culture dishes were purchased from Himedia. Tris-Acetate EDTA (TAE), Acrylamide/bis(acrylamide) sol 30% were purchased from GeNei. Magnesium chloride was ordered from SRL, India. Galectin-3 was provided as a gift from the Johannes team at Institut Curie, Paris.

4.2. Synthesis of DNs. The synthesis of TD³⁰ and BB²⁹ was done by one-pot synthesis. The primers were reconstituted in nuclease free water to 100 μ M stock and diluted to 10 μ M working concentration. DNA TD was synthesized using four oligonucleotides mixed in equimolar ratios (T1:T2: T3:T4–1:1:1:1) (Table S1, Supporting Information) containing 2 mM MgCl₂. BB was synthesized using L (long), M (medium), and S (small) strands. For BB, the L:M:S ratio was 1:3:3 with 2 mM MgCl₂ (Table S3, Supporting Information). The reaction was carried out in a thermocycler, and the reaction mixture was heated to 95 °C and then gradually cooled to 4 °C. The reaction cycle has a 5 °C step decrease with an interval of 15 min at every step. The final concentration for TD and BB was 1 and 1.1 μ M, respectively.

The synthesis of ID and cube was done through modular assembly. For ID, three 5WJ were formed in the first step (V₅, U₅, and L₅) with an equimolar ratio of the primers (Table S2, Supporting Information), and 2 mM MgCl₂ was added. In the second step, one part of V₅ was combined with 5 parts of U₅ and L₅, each forming two half icosahedrons (VU₅ and VL₅). This reaction was also carried out in the presence of MgCl₂. The last step is 1:1 assembly of VU₅ and VL₅. The first step was performed on 95 to 4 °C, similar to one pot assembly. The second and third step use the temperature 45 °C decreasing to 4 °C with 5 °C decrease in each step for 30 min. For cube, the first step creates Tile A (L:SA:MA – 1:3:3) and Tile B (L:SB:MB – 1:3:3) with 2 mM MgCl₂ (Table S4, Supporting Information). The annealing conditions were like the one-pot reaction. The second step is a 1:1 mixture of Tile A and Tile B, and the reaction condition was similar to the second and third step of ID assembly. The final concentration of ID and cube were 1.6 and 1.1 μ M, respectively. All the structures were stored at 4 °C until further use.

4.3. Characterization of DNs. **4.3.1. Electrophoretic Mobility Shift Assay (EMSA).** The size-based characterization was done using three methods. Electrophoretic mobility shift assay (EMSA) was performed using Native-PAGE. 5% polyacrylamide gel was prepared to study the higher order structure formation. The sample contained 5 μ L of DNA nanostructure sample with 3 μ L of loading buffer and 1.5 μ L of 6× loading dye. The gel was run on 80 V for 80 min. The gel was stained with EtBr stain and visualized using Gel Documentation system (Biorad ChemiDoc MP Imaging System).

4.3.2. Dynamic Light Scattering (DLS). The size-based characterization of DNs was done to measure the hydrodynamic size of the formed structures using Dynamic Light Scattering (DLS). The sample was diluted in a 1:20 ratio, and 50 μ L of samples was used to analyze the hydrodynamic radius using the Malvern analytical Zetasizer Nano ZS instrument. The readings were taken in triplicates, with 13 readings in one run.

4.3.3. Atomic Force Microscopy (AFM). The morphology-based characterization was performed using Atomic Force Microscopy. A freshly cleaved mica was treated with 1 mM NiCl₂ solution for 15 min and then washed 2 times with ultrapure water. 20–30 μ L droplets of DNA nanostructure samples (150 nM) were then overlaid on top and were incubated for 15 min. The excess sample was then drained and washed 2 times with ultrapure water and was dried and imaged using MPF-3D BIO AFM (Asylum Research, Oxford Instruments) in tapping mode in air. A sharp silicon cantilever AC160TS (Olympus) was used for AFM imaging.

4.4. In Vitro Studies. **4.4.1. Cell Culture.** HeLa (Cervical Cancer), MDA-MB-231 (Breast Cancer), Rpe1 (Retinal pigment epithelial cells), HEK293T (Human Embryonic Kidney cells), KB3 (Oral Cancer) cells were maintained in DMEM, SUM-159-A (Breast Cancer) cells were maintained in HAMS-F12 media, and SHSYSY (Human Neuroblastoma) were maintained in DMEM-F12. All the media were supplemented with 10% fetal bovine serum and 1% penicillin/streptomycin. The cells were maintained at 37 °C with 5% CO₂ in a humidified incubator.

4.4.2. Cellular Uptake Assay. For cellular uptake experiments, all the cells were maintained in their respective media as described previously. Cells were seeded at a density of 0.1 × 10⁶ cells/well on 18 mm glass coverslips in 12 well plates 24 h before the experiment. Before experiments, cells were checked on the microscope to visualize

their proper attachment and spreading. Cells were washed twice with 1× PBS and then incubated with serum-free media containing different concentrations of DNAs and 5 μg/mL of Tf-A488 for concentration-dependent and cell-type specific experiments. The cells were incubated at 37 °C for 20 min and then washed twice with acid buffer (pH 2.5) followed by three times washing with 1× PBS to remove the excess or surface bound DNAs. The cells were fixed using 4% paraformaldehyde for 15 min at 37 °C. The cells were again washed thrice with 1× PBS and mounted on the glass slide using Mowiol containing Hoechst to mark the nucleus.

4.4.3. Inhibitor Studies. The endocytosis inhibitor study was performed to understand the pathway by which nanostructures are being uptaken. Rpe1 cells were seeded into 12-well plate on coverslips and grown until 80–90% confluency. The cells were washed with PBS and preincubated with Pitstop (20 μM, 40 μM) or Dynasore (60, 80, 100 μM) or Lactose (100, 150, 200 mM) in serum free DMEM for 15 min at 37 °C. The media was decanted, and the cells were treated with the same concentration of inhibitors with transferrin-A488 (5 μg/mL), galectin3-Cy5 (5 μg/mL), and TD (150 nM) in serum free DMEM. The cells were incubated at 37 °C for 15 min. The cells were then washed with PBS and fixed with 4% PFA at 37 °C for 15 min. They were washed with PBS and mounted with Mowiol and Hoechst to mark the nucleus.

4.4.4. 3D Spheroid Invasion Assay. MDA-MB231 cells were used to prepare 3D spheroids using the *hanging-drop method*. The cells were trypsinized, and an appropriate volume of complete media was added. 2.5×10^4 cells were taken in total 50 μL of complete media and seeded in droplet form on the lid of a Petri dish. The base of the Petri dish was filled with 15 mL of PBS to provide humidity for spheroid growth. The cells were incubated at 37 °C for 36 h. The cells clumped together and aggregated due to gravity to form spheroids. The spheroid formation was confirmed by observation under a bright field optical microscope. The spheroids were transferred to 12 well plates using 3:1 collagen to media proportion containing collagen covered coverslips, and it was incubated at 37 °C for 1 h. The spheroids were then incubated with different nanostructures at 150 nM in serum free media for 24 h at 37 °C. The spheroids were fixed using 4% PFA for 15 min at 37 °C. For phalloidin staining, spheroids were first permeabilized using 0.1% TritonX and incubated for 10 min at room temperature. After that 0.1× TritonX+Phalloidin solution (1:1000 dilution) was added and incubated at 37 °C for 30 min. Spheroids were washed gently twice with 1× PBS and mounted using Mowiol+Hoechst.

4.4.5. Confocal Microscopy. Fixed cells were imaged using a Confocal Scanning Laser Microscope (Leica TCS SP8). The 2D cell culture assay slides were imaged using a 63× oil immersion objective, while the 3D cell culture (spheroids) assay slides were imaged using 10× and 20× objectives. The pinhole was kept 1 Airy unit. Different fluorophores were excited using different lasers, i.e., for Hoechst 405 nm, Tf-A488:488 nm, TD-Cy3:561 nm, and Gal3-Cy5 633 nm. The image analysis was done using Fiji ImageJ software.^{33,49,50} The background from each image was subtracted using Fiji ImageJ software (NIH), and whole cell intensity was quantified using maximum intensity projection. The autofluorescence of the cells was eliminated by quantifying the signal from the unlabeled cells. For each sample 4–5 z-stacks were taken and 35–45 cells were quantified to study the cellular experiments. For comparison of cellular uptake of DNAs, the fluorescence intensity from cells was normalized with respect to the blank control where the signal from the nontreated cell was considered as 100. However, for the different number of fluorophores per cage in case of cube and BB, the whole cell intensity was divided by the number of fluorophores.

4.5. In Vivo Study. **4.5.1. Fish Strain.** All experiments were done in the *Tg(cldb::lym-EGFP)* strain,⁵¹ which marked the plasma membrane and helped in its visualization. For zebrafish maintenance and experimentation, guidelines recommended by the Committee for the Purpose of Control and Supervision of Experiments on Animals (CPCSEA), Govt. of India, were followed.

4.5.2. DNA Nanostructure Treatment and Fixation. For the uptake of DNA nanocages, larvae at 72 hpf were incubated in 300 nM

nanocage solution in E3 medium without methylene blue. To visualize the vesicles, Alexa Fluor 647 conjugated Wheat Gram Agglutinin at the concentration of 5 μg/mL was used as a tracer. The larvae were pulsed in this solution for 4 h followed by E3 (without methylene blue) washes and were then fixed in 4% PFA in PEMTT buffer (0.1 M PIPES, 5 mM EGTA, 2 mM MgCl₂·6H₂O, 0.1% TritonX-100, 0.1% Tween 20, pH 6.8).⁵² Larvae pulsed with only tracer were used as control. The fixed embryos were kept overnight at 4 °C, followed by glycerol upgrade and storage at 4 °C.

4.5.3. Image Acquisition and Processing. Imaging was performed over the head (dorsal head periderm) of zebrafish larvae using Zeiss LSM 880 confocal microscope with an EC Plan 63×/1.40 oil immersion objective lens at 1.5× optical zoom with a Z-step of 0.37 μm. The images were taken at a resolution of 1024 × 1024. The pinhole values were kept at 1 Airy Unit. The PMT and laser power were kept constant while imaging the nanocages. Fiji ImageJ was used for image processing and analysis.⁵³

5. STATISTICAL ANALYSIS

For in vitro studies, the uptake of different DNAs in cells was quantified from the background subtracted cells using ImageJ software (NIH) and the image quantification using Graphpad Prism 8.0. For in vivo studies, the total number of WGA vesicles and the vesicles colocalizing with the nanocages were counted manually and plotted. Experiments were not randomized. The investigators were not blinded to allocation during experiments and outcome. Mean values with associated standard deviation (SD) or standard error (SE) were used and are mentioned accordingly in the main manuscript. *p* values were calculated using one-way ANOVA and two-tailed unpaired *t* tests on GraphPad Prism (confidence interval: 95%).

ASSOCIATED CONTENT

Supporting Information

The Supporting Information is available free of charge at <https://pubs.acs.org/doi/10.1021/acsnano.2c01382>.

Additional experiments and the details about the sequences of the oligonucleotides used, the stability of the DNA nanostructures (S1) and additional characterization using AFM (S14, S16), titration of DNA BB and DNA cube (S2 and S3), linear regression analysis to check the concentration dependent uptake of DNA TD (S15), experiments showing the uptake of DNA nanostructures in different cell lines (S4–S8), inhibitor studies in different cell line and effect of blocking the caveolin pathway on the uptake of DNA TD (S9–S11), uptake of ssDNA and free cyanine dye (S12, S13) (PDF)

AUTHOR INFORMATION

Corresponding Author

Dhiraj Bhatia – Biological Engineering and Center for Biomedical Engineering, Indian Institute of Technology Gandhinagar, Gandhinagar, Gujarat 382355, India; orcid.org/0000-0002-1478-6417; Email: dhiraj.bhatia@iitgn.ac.in

Authors

Anjali Rajwar – Biological Engineering, Indian Institute of Technology Gandhinagar, Gandhinagar, Gujarat 382355, India

Shravani Reddy Shetty – Department of Biological Sciences, Tata Institute of Fundamental Research, Mumbai 400005, India

Payal Vaswani – Biological Engineering, Indian Institute of Technology Gandhinagar, Gandhinagar, Gujarat 382355, India

Vinod Morya – Biological Engineering, Indian Institute of Technology Gandhinagar, Gandhinagar, Gujarat 382355, India; orcid.org/0000-0002-1539-4108

Amlan Barai – Bioscience and Bioengineering Department, Indian Institute of Technology Bombay, Mumbai 400076, India

Shamik Sen – Bioscience and Bioengineering Department, Indian Institute of Technology Bombay, Mumbai 400076, India

Mahendra Sonawane – Department of Biological Sciences, Tata Institute of Fundamental Research, Mumbai 400005, India

Complete contact information is available at:
<https://pubs.acs.org/10.1021/acsnano.2c01382>

Notes

The authors declare no competing financial interest. The preprint version of this article is available on bioRxiv as follows: Gada, A. R.; Rs, S.; Vaswani, P.; Morya, V.; Barai, A.; Sen, S.; Gupta, S.; Sonawane, M.; Bhatia, D. Ligand Geometry Dictates Cellular and in Vivo Uptake of 3D DNA Nanostructures. *bioRxiv*, October 20, 2021, 2021.10.19.465062. DOI: [10.1101/2021.10.19.465062](https://doi.org/10.1101/2021.10.19.465062).

ACKNOWLEDGMENTS

We sincerely thank all the members of the DB group for critically reading the manuscript and their valuable feedback. AR, VM thank IITGN-MHRD, GoI for PhD fellowships. PV acknowledges a PhD fellowship from UGC-CSIR, India and IITGN for additional fellowship. DB thanks SERB, GoI for Ramanujan Fellowship, IITGN, for the startup grant, and DBT-EMR, Gujcost-DST, GSBTM, and BRNS-BARC for research grants. We sincerely thank Dr. Ramesh for his kind and timely help with the AFM. MS acknowledges the support from TIFR-DAE (RTI4003;12P-121). Imaging facilities of CIF at IIT Gandhinagar are acknowledged.

REFERENCES

- (1) Seeman, N. C. DNA in a Material World. *Nature* **2003**, *421* (6921), 427–431.
- (2) Rothemund, P. W. K. Folding DNA to Create Nanoscale Shapes and Patterns. *Nature* **2006**, *440* (7082), 297–302.
- (3) Benson, E.; Mohammed, A.; Gardell, J.; Masich, S.; Czeizler, E.; Orponen, P.; Högberg, B. DNA Rendering of Polyhedral Meshes at the Nanoscale. *Nature* **2015**, *523* (7561), 441–444.
- (4) Douglas, S. M.; Marblestone, A. H.; Theerapittayanon, S.; Vazquez, A.; Church, G. M.; Shih, W. M. Rapid Prototyping of 3D DNA-Origami Shapes with CaDNAno. *Nucleic Acids Res.* **2009**, *37* (15), 5001–5006.
- (5) Yan, J.; Hu, C.; Wang, P.; Zhao, B.; Ouyang, X.; Zhou, J.; Liu, R.; He, D.; Fan, C.; Song, S. Growth and Origami Folding of DNA on Nanoparticles for High-Efficiency Molecular Transport in Cellular Imaging and Drug Delivery. *Angew. Chem.* **2015**, *127* (8), 2461–2465.
- (6) Liu, J.; Song, L.; Liu, S.; Zhao, S.; Jiang, Q.; Ding, B. A Tailored DNA NanoplatforM for Synergistic RNAi-/Chemotherapy of Multi-drug-Resistant Tumors. *Angew. Chem., Int. Ed.* **2018**, *57* (47), 15486–15490.

- (7) Rajwar, A.; Kharbanda, S.; Chandrasekaran, A. R.; Gupta, S.; Bhatia, D. Designer, Programmable 3D DNA Nanodevices to Probe Biological Systems. *ACS Appl. Bio Mater.* **2020**, *3* (11), 7265–7277.
- (8) Chang, M.; Yang, C.-S.; Huang, D.-M. Aptamer-Conjugated DNA Icosahedral Nanoparticles As a Carrier of Doxorubicin for Cancer Therapy. *ACS Nano* **2011**, *5* (8), 6156–6163.
- (9) Banerjee, A.; Bhatia, D.; Saminathan, A.; Chakraborty, S.; Kar, S.; Krishnan, Y. Controlled Release of Encapsulated Cargo from a DNA Icosahedron Using a Chemical Trigger. *Angew. Chem., Int. Ed. Engl.* **2013**, *52* (27), 6854–6857.
- (10) Douglas, S. M.; Bachelet, I.; Church, G. M. A Logic-Gated Nanorobot for Targeted Transport of Molecular Payloads. *Science* **2012**, *335* (6070), 831–834.
- (11) Xie, X.; Shao, X.; Ma, W.; Zhao, D.; Shi, S.; Li, Q.; Lin, Y. Overcoming Drug-Resistant Lung Cancer by Paclitaxel Loaded Tetrahedral DNA Nanostructures. *Nanoscale* **2018**, *10* (12), 5457–5465.
- (12) Walsh, A. S.; Yin, H.; Erben, C. M.; Wood, M. J. A.; Turberfield, A. J. DNA Cage Delivery to Mammalian Cells. *ACS Nano* **2011**, *5* (7), 5427–5432.
- (13) Zhang, Q.; Jiang, Q.; Li, N.; Dai, L.; Liu, Q.; Song, L.; Wang, J.; Li, Y.; Tian, J.; Ding, B.; Du, Y. DNA Origami as an In Vivo Drug Delivery Vehicle for Cancer Therapy. *ACS Nano* **2014**, *8* (7), 6633–6643.
- (14) Jiang, Q.; Song, C.; Nangreave, J.; Liu, X.; Lin, L.; Qiu, D.; Wang, Z.-G.; Zou, G.; Liang, X.; Yan, H.; Ding, B. DNA Origami as a Carrier for Circumvention of Drug Resistance. *J. Am. Chem. Soc.* **2012**, *134* (32), 13396–13403.
- (15) Halley, P. D.; Lucas, C. R.; McWilliams, E. M.; Webber, M. J.; Patton, R. A.; Kural, C.; Lucas, D. M.; Byrd, J. C.; Castro, C. E. Daunorubicin-Loaded DNA Origami Nanostructures Circumvent Drug-Resistance Mechanisms in a Leukemia Model. *Small* **2016**, *12* (3), 308–320.
- (16) Li, S.; Jiang, Q.; Liu, S.; Zhang, Y.; Tian, Y.; Song, C.; Wang, J.; Zou, Y.; Anderson, G. J.; Han, J.-Y.; Chang, Y.; Liu, Y.; Zhang, C.; Chen, L.; Zhou, G.; Nie, G.; Yan, H.; Ding, B.; Zhao, Y. A DNA Nanorobot Functions as a Cancer Therapeutic in Response to a Molecular Trigger in Vivo. *Nat. Biotechnol.* **2018**, *36* (3), 258–264.
- (17) Cremers, G. A. O.; Rosier, B. J. H. M.; Riera Brillas, R.; Albertazzi, L.; de Greef, T. F. A. Efficient Small-Scale Conjugation of DNA to Primary Antibodies for Multiplexed Cellular Targeting. *Bioconjugate Chem.* **2019**, *30* (9), 2384–2392.
- (18) Setyawati, M. I.; Kutty, R. V.; Leong, D. T. DNA Nanostructures Carrying Stoichiometrically Definable Antibodies. *Small* **2016**, *12* (40), 5601–5611.
- (19) Ranallo, S.; Prévost-Tremblay, C.; Idili, A.; Vallée-Bélisle, A.; Ricci, F. Antibody-Powered Nucleic Acid Release Using a DNA-Based Nanomachine. *Nat. Commun.* **2017**, *8* (1), 15150.
- (20) Liu, Q.; Wang, D.; Xu, Z.; Huang, C.; Zhang, C.; He, B.; Mao, C.; Wang, G.; Qian, H. Targeted Delivery of Rab26 siRNA with Precisely Tailored DNA Prism for Lung Cancer Therapy. *ChemBioChem.* **2019**, *20* (9), 1139–1144.
- (21) Schüller, V. J.; Heidegger, S.; Sandholzer, N.; Nickels, P. C.; Suhartha, N. A.; Endres, S.; Bourquin, C.; Liedl, T. Cellular Immunostimulation by CpG-Sequence-Coated DNA Origami Structures. *ACS Nano* **2011**, *5* (12), 9696–9702.
- (22) Thai, H. B. D.; Kim, K.-R.; Hong, K. T.; Voitsitskiy, T.; Lee, J.-S.; Mao, C.; Ahn, D.-R. Kidney-Targeted Cytosolic Delivery of siRNA Using a Small-Sized Mirror DNA Tetrahedron for Enhanced Potency. *ACS Cent. Sci.* **2020**, *6* (12), 2250–2258.
- (23) Bastings, M. M. C.; Anastassacos, F. M.; Ponnuswamy, N.; Leifer, F. G.; Cuneo, G.; Lin, C.; Ingber, D. E.; Ryu, J. H.; Shih, W. M. Modulation of the Cellular Uptake of DNA Origami through Control over Mass and Shape. *Nano Lett.* **2018**, *18* (6), 3557–3564.
- (24) Wang, P.; Rahman, M. A.; Zhao, Z.; Weiss, K.; Zhang, C.; Chen, Z.; Hurwitz, S. J.; Chen, Z. G.; Shin, D. M.; Ke, Y. Visualization of the Cellular Uptake and Trafficking of DNA Origami Nanostructures in Cancer Cells. *J. Am. Chem. Soc.* **2018**, *140* (7), 2478–2484.

- (25) Jiang, D.; Ge, Z.; Im, H.-J.; England, C. G.; Ni, D.; Hou, J.; Zhang, L.; Kuttyreff, C. J.; Yan, Y.; Liu, Y.; Cho, S. Y.; Engle, J. W.; Shi, J.; Huang, P.; Fan, C.; Yan, H.; Cai, W. DNA Origami Nanostructures Can Exhibit Preferential Renal Uptake and Alleviate Acute Kidney Injury. *Nat. Biomed Eng.* **2018**, *2* (11), 865–877.
- (26) Goodman, R. P.; Berry, R. M.; Turberfield, A. J. The Single-Step Synthesis of a DNA Tetrahedron. *Chem. Commun.* **2004**, No. 12, 1372–1373.
- (27) Bhatia, D.; Mehtab, S.; Krishnan, R.; Indi, S. S.; Basu, A.; Krishnan, Y. Icosahedral DNA Nanocapsules by Modular Assembly. *Angew. Chem., Int. Ed.* **2009**, *48* (23), 4134–4137.
- (28) Zhang, C.; Ko, S. H.; Su, M.; Leng, Y.; Ribbe, A. E.; Jiang, W.; Mao, C. Symmetry Controls the Face Geometry of DNA Polyhedra. *J. Am. Chem. Soc.* **2009**, *131* (4), 1413–1415.
- (29) He, Y.; Ye, T.; Su, M.; Zhang, C.; Ribbe, A. E.; Jiang, W.; Mao, C. Hierarchical Self-Assembly of DNA into Symmetric Supramolecular Polyhedra. *Nature* **2008**, *452* (7184), 198–201.
- (30) Goodman, R. P.; Schaap, I. a. T.; Tardin, C. F.; Erben, C. M.; Berry, R. M.; Schmidt, C. F.; Turberfield, A. J. Rapid Chiral Assembly of Rigid DNA Building Blocks for Molecular Nanofabrication. *Science* **2005**, *310* (5754), 1661–1665.
- (31) Peng, X.; Fang, S.; Ji, B.; Li, M.; Song, J.; Qiu, L.; Tan, W. DNA Nanostructure-Programmed Cell Entry via Corner Angle-Mediated Molecular Interaction with Membrane Receptors. *Nano Lett.* **2021**, *21* (16), 6946–6951.
- (32) Lacroix, A.; Vengut-Climent, E.; de Rochambeau, D.; Sleiman, H. F. Uptake and Fate of Fluorescently Labeled DNA Nanostructures in Cellular Environments: A Cautionary Tale. *ACS Cent. Sci.* **2019**, *5* (5), 882–891.
- (33) Smolková, B.; MacCulloch, T.; Rockwood, T. F.; Liu, M.; Henry, S. J. W.; Frtús, A.; Uzhychak, M.; Lunova, M.; Hof, M.; Jurkiewicz, P.; Dejneka, A.; Stephanopoulos, N.; Lunov, O. Protein Corona Inhibits Endosomal Escape of Functionalized DNA Nanostructures in Living Cells. *ACS Appl. Mater. Interfaces* **2021**, *13* (39), 46375–46390.
- (34) Modi, S.; Swetha, M. G.; Goswami, D.; Gupta, G. D.; Mayor, S.; Krishnan, Y. A DNA Nanomachine That Maps Spatial and Temporal PH Changes inside Living Cells. *Nat. Nanotechnol.* **2009**, *4* (5), 325–330.
- (35) Surana, S.; Bhat, J. M.; Koushika, S. P.; Krishnan, Y. An Autonomous DNA Nanomachine Maps Spatiotemporal PH Changes in a Multicellular Living Organism. *Nat. Commun.* **2011**, *2* (1), 340.
- (36) Bhatia, D.; Surana, S.; Chakraborty, S.; Koushika, S. P.; Krishnan, Y. A Synthetic Icosahedral DNA-Based Host–Cargo Complex for Functional in Vivo Imaging. *Nat. Commun.* **2011**, *2* (1), 339.
- (37) von Kleist, L.; Stahlschmidt, W.; Bulut, H.; Gromova, K.; Puchkov, D.; Robertson, M. J.; MacGregor, K. A.; Tomilin, N.; Pechstein, A.; Chau, N.; Chircop, M.; Sakoff, J.; von Kries, J. P.; Saenger, W.; Kräusslich, H.-G.; Shupliakov, O.; Robinson, P. J.; McCluskey, A.; Haucke, V. Role of the Clathrin Terminal Domain in Regulating Coated Pit Dynamics Revealed by Small Molecule Inhibition. *Cell* **2011**, *146* (3), 471–484.
- (38) Lakshminarayan, R.; Wunder, C.; Becken, U.; Howes, M. T.; Benzing, C.; Arumugam, S.; Sales, S.; Ariotti, N.; Chambon, V.; Lamaze, C.; Loew, D.; Shevchenko, A.; Gaus, K.; Parton, R. G.; Johannes, L. Galectin-3 Drives Glycosphingolipid-Dependent Biogenesis of Clathrin-Independent Carriers. *Nat. Cell Biol.* **2014**, *16* (6), 592–603.
- (39) Macia, E.; Ehrlich, M.; Massol, R.; Boucrot, E.; Brunner, C.; Kirchhausen, T. Dynasore, a Cell-Permeable Inhibitor of Dynamin. *Developmental Cell* **2006**, *10* (6), 839–850.
- (40) Mathew, M. P.; Donaldson, J. G. Distinct Cargo-Specific Response Landscapes Underpin the Complex and Nuanced Role of Galectin-Glycan Interactions in Clathrin-Independent Endocytosis. *J. Biol. Chem.* **2018**, *293* (19), 7222–7237.
- (41) Harvey, R. D.; Calaghan, S. C. Caveolae Create Local Signalling Domains through Their Distinct Protein Content, Lipid Profile and Morphology. *Journal of Molecular and Cellular Cardiology* **2012**, *52* (2), 366–375.
- (42) Orlandi, P. A.; Fishman, P. H. Filipin-Dependent Inhibition of Cholera Toxin: Evidence for Toxin Internalization and Activation through Caveolae-like Domains. *J. Cell Biol.* **1998**, *141* (4), 905–915.
- (43) Timmins, N.; Dietmair, S.; Nielsen, L. Hanging-Drop Multicellular Spheroids as a Model of Tumour Angiogenesis. *Angiogenesis* **2004**, *7* (2), 97–103.
- (44) Shi, S.; Peng, Q.; Shao, X.; Xie, J.; Lin, S.; Zhang, T.; Li, Q.; Li, X.; Lin, Y. Self-Assembled Tetrahedral DNA Nanostructures Promote Adipose-Derived Stem Cell Migration via LncRNA XLOC 010623 and RHOA/ROCK2 Signal Pathway. *ACS Appl. Mater. Interfaces* **2016**, *8* (30), 19353–19363.
- (45) Zhao, D.; Liu, M.; Li, Q.; Zhang, X.; Xue, C.; Lin, Y.; Cai, X. Tetrahedral DNA Nanostructure Promotes Endothelial Cell Proliferation, Migration, and Angiogenesis via Notch Signaling Pathway. *ACS Appl. Mater. Interfaces* **2018**, *10* (44), 37911–37918.
- (46) Ma, W.; Xie, X.; Shao, X.; Zhang, Y.; Mao, C.; Zhan, Y.; Zhao, D.; Liu, M.; Li, Q.; Lin, Y. Tetrahedral DNA Nanostructures Facilitate Neural Stem Cell Migration via Activating RHOA/ROCK2 Signalling Pathway. *Cell Proliferation* **2018**, *51* (6), e12503.
- (47) Elkhatib, N.; Bresteau, E.; Baschieri, F.; Rioja, A. L.; van Niel, G.; Vassilopoulos, S.; Montagnac, G. Tubular Clathrin/AP-2 Lattices Pinch Collagen Fibers to Support 3D Cell Migration. *Science* **2017**, DOI: 10.1126/science.aal4713.
- (48) Smith, J.; Yu, R.; Hinkle, P. M. Activation of MAPK by TRH Requires Clathrin-Dependent Endocytosis and PKC but Not Receptor Interaction with β -Arrestin or Receptor Endocytosis. *Mol. Endocrinol.* **2001**, *15* (9), 1539–1548.
- (49) Bankhead, P. *Analyzing Fluorescence Microscopy Images with ImageJ*; Queens University, 2014.
- (50) Bhatia, D.; Arumugam, S.; Nasilowski, M.; Joshi, H.; Wunder, C.; Chambon, V.; Prakash, V.; Grazon, C.; Nadal, B.; Maiti, P. K.; Johannes, L.; Dubertret, B.; Krishnan, Y. Quantum Dot-Loaded Monofunctionalized DNA Icosahedra for Single-Particle Tracking of Endocytic Pathways. *Nat. Nanotechnol.* **2016**, *11* (12), 1112–1119.
- (51) Haas, P.; Gilmour, D. Chemokine Signaling Mediates Self-Organizing Tissue Migration in the Zebrafish Lateral Line. *Developmental Cell* **2006**, *10* (5), 673–680.
- (52) Song, S.; Eckerle, S.; Onichtchouk, D.; Marrs, J. A.; Nitschke, R.; Driever, W. Pou5f1-Dependent EGF Expression Controls E-Cadherin Endocytosis, Cell Adhesion, and Zebrafish Epiboly Movements. *Developmental Cell* **2013**, *24* (5), 486–501.
- (53) Schindelin, J.; Arganda-Carreras, I.; Frise, E.; Kaynig, V.; Longair, M.; Pietzsch, T.; Preibisch, S.; Rueden, C.; Saalfeld, S.; Schmid, B.; Tinevez, J.-Y.; White, D. J.; Hartenstein, V.; Eliceiri, K.; Tomancak, P.; Cardona, A. Fiji: An Open-Source Platform for Biological-Image Analysis. *Nat. Methods* **2012**, *9* (7), 676–682.